AIAA JOURNAL
Vol. 39, No. 8, August 2001

Chapman–Jouguet Oblique Detonation Structure Around Hypersonic Projectiles

Jiro Kasahara*
Muroran Institute of Technology, Muroran 050-8585, Japan
Toshi Fujiwara† and Takuma Endo‡
Nagoya University, Nagoya 464-8603, Japan
and
Takakage Arai§
Muroran Institute of Technology, Muroran 050-8585, Japan

How to generate a steady-state detonation around a hypersonic projectile in stoichiometric hydrogen-oxygen premixed gases is studied. The speed of the hypersonic projectiles was beyond the Chapman–Jouguet (C–J) detonation speed. The flowfield around the projectile was visualized by using a gate intensified charge-coupled device camera (single-frame schlieren pictures and OH radical self-emission images). Three parameters are varied: 1) the projectile flight length from diaphragm rupture location, 2) the initial pressure of mixture below/above the critical pressure for steady detonation initiation around a hypersonic projectile, and 3) the projectile speed. At the pressure condition below the criteria, the detonation structure is composed of three different shock and detonation waves, which appear just after a diaphragm rupture and evolve in time: an overdriven bow detonation wave, a strong detonation wave, and a diffracted shock wave. Their propagation after diaphragm rupture is investigated, and it is found that the C–J detonation wave moved away from the projectile and only a reactive bow shock wave remained around projectile far away from the diaphragm. At the pressure condition above the criteria, a steady oblique detonation wave was generated around the projectile as soon as the projectile broke the diaphragm. In this steady-state detonation-wave case, with respect to the flow Mach number behind the wave front, the whole detonation wave was divided into four parts: 1) strong overdriven detonation wave, 2) weak overdriven detonation wave, 3) quasi-C–J detonation wave, and 4) C–J detonation wave. It has been found that a rarefaction wave is generated at the projectile shoulder and that curvature of the wave has a significant effect on the structure of the detonation wave.

Introduction

FOR many years, combustion phenomena around hypersonic projectile have been studied experimentally by Zel'dovich and Leipunsky,[1] Ruegg and Dorsey,[2] McVey and Toong,[3] Lehr,[4] and Alpert and Toong,[5] recently numerically by Matsuo and Fujii,[6,7] and experimentally by Kamel et al.[8] In their cases, the interaction between the shock wave and chemical reaction around projectiles was weak. Two-dimensional steady oblique detonation waves were experimentally and numerically investigated in the extensive work of Viguier et al.,[9] Debordes et al.,[10] and Li et al.[11] Higgins,[12] Higgins and Bruckner,[13] and Higgins[14] concentrated on the criteria of detonation initiation by projectiles. Lee[15] investigated the initiation conditions by using the cylindrical strong blast wave analogy. The initiation conditions by hypersonic projectiles were explained by his analysis, but many questions about the steady-state oblique detonation structure remained unsolved. Because there were few studies of the strong interaction,[16] we have been studying the oblique detonation waves generated around ballistic-range projectiles in H_2–O_2 and H_2–air mixtures.[17–19] Experimental studies of oblique detonation waves are not only interesting in themselves, but also important for the stable operation of new hypersonic propulsion applications,[20] such as ram accelerators,[21] oblique detonation wave engines,[22] and pulse detonation engines.[23]

In the present study, we explore how a steady-state detonation develops around a hypersonic projectile. We varied three parameters: 1) the projectile flight lengths from diaphragm rupture location, 2) the initial pressure of mixture below/above the critical pressure for the steady detonation initiation around a hypersonic projectile, and 3) the projectile speed. By using single-frame schlieren pictures and OH radical self-emission images, we captured the shock (or detonation) waves propagating around the projectile after the diaphragm rupture.

Experimental Facility and Conditions

The schematic diagram of the experimental arrangement (top view) is shown in Fig. 1. The experimental equipment is composed of four elements: 1) a two-stage, light-gas gun to launch a hypersonic projectile, 2) a combustion chamber containing the gas mixture, 3) an imaging system, which consisted of either a schlieren system or an OH-emission imaging system (using an interference filter) for observation, and 4) an evacuation chamber for releasing the projectile and burned gas.

The two-stage, light-gas gun[24] uses high-pressure air, at 5 MPa, to drive the piston. The driver gas is helium. The maximum projectile speed achievable with this gun is 5 km/s. A stainless-steel, cylindrical tube of 145-mm internal diameter, 690-mm length and 10-mm thickness contains the hydrogen–oxygen mixture. This combustion chamber has a 160-mm observation window on the vertical plane, perpendicular to the centerline of the tube. The position of the projectile is determined by a He–Ne laser cutting signal. About 30 μs after the detection, the projectile arrives at the objective location and the imaging system records the flowfield around the projectile. After the combustion chamber, the projectile breaks a Mylar® film, and it impacts aluminum plate in the evacuation chamber, which consists of a cylinder of 1.0-m diam and 2.0-m^3 volume, and is ready when the pressure drops to 100 Pa. As soon as the projectile breaks the diaphragm, the high-pressure burned gas is exhausted into the evacuation chamber, so that the combustion chamber is not exposed to

Received 25 July 2000; revision received 16 January 2001; accepted for publication 8 March 2001.

*Research Associate, Department of Mechanical Systems Engineering, Mizumoto-cho 27-1; kasahara@mmm.muroran-it.ac.jp. Member AIAA.

†Professor, Department of Aerospace Engineering, Chikusa-ku, Furo-cho; toshi@nuae.nagoya-u.ac.jp.

‡Associate Professor, Center for Integrated Research in Science and Engineering, Chikusa-ku, Furo-cho; endo@cirse.nagoya-u.ac.jp.

§Associate Professor, Department of Mechanical Systems Engineering, Mizumoto-cho 27-1; arai@mmm.muroran-it.ac.jp. Senior Member AIAA.

Table 1 Experimental conditions of Figs. 3, 4, and 7

Figure	Projectile location, mm	Diaphragm thickness, μm	T_0, K	p_0, atm	V_p, km/s
3a	35 ± 8	12	299.1 ± 0.4	0.203 ± 0.003	3.64 ± 0.13
3b	134 ± 8	12	299.6 ± 0.4	0.335 ± 0.003	3.29 ± 0.13
3c	267 ± 30	12	301.1 ± 0.4	0.334 ± 0.003	3.27 ± 0.07
3d	442 ± 50	50	302.6 ± 0.4	0.334 ± 0.003	3.66 ± 0.23
4	205 ± 8	12	296.1 ± 0.4	0.334 ± 0.003	3.35 ± 0.17
7a	68 ± 8	12	299.9 ± 0.4	0.506 ± 0.003	3.42 ± 0.13
7b	326 ± 8	50	302.2 ± 0.4	0.506 ± 0.003	3.71 ± 0.24

Table 2 Experimental conditions of Fig. 17

Figure	T_0, K	p_0, atm	V_p, km/s
17a	294.4 ± 0.4	0.392 ± 0.003	2.91 ± 0.10
17b	295.1 ± 0.4	0.389 ± 0.003	3.49 ± 0.11
17c	295.2 ± 0.4	0.390 ± 0.003	3.76 ± 0.13
17d	295.7 ± 0.4	0.390 ± 0.003	4.12 ± 0.13

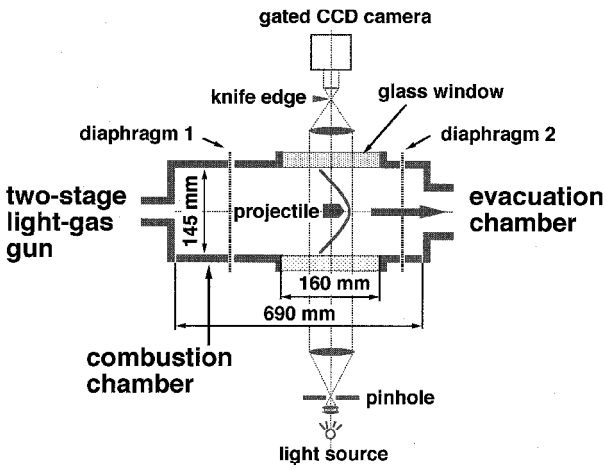

Fig. 1 Schematic diagram of the experimental arrangement (top view).

high pressure for a long time. The total time for the operation, from releasing high-pressure air in the gas gun to impact of the projectile in the evacuation chamber, is about 1 ms.

The schlieren system for visualizing the flowfield around the projectile uses a flash lamp with spark duration of 2 μs. The pinhole diameter was 0.5 mm. The objective lens was a spherical convex lens 150 mm in diameter. The knife edge was placed as shown in Fig. 1. A high-speed gate intensified charge-coupled device (ICCD) camera unit C5987 (Hamamatsu Photonics K. K.) was used. Exposure time was 100 ns (except as indicated). The spatial resolution was approximately 0.1 mm at the objective plane. The camera and light source were triggered by the laser cutting signal described earlier. This trigger signal was delayed by a digital delay generator DG535 (Stanford Research Systems).

These experimental conditions are shown in Tables 1 and 2 or described in the text. We performed the experiments in a stoichiometric hydrogen–oxygen gas mixture at initial fill pressures from 0.10 to 0.52 atm and room temperature of about 300 K. The projectiles had a conical nose of 120 deg open angle (except as indicated), 10 mm in diameter, and were made of polyethylene. The projectile velocity was one of the variables in the set of experiments, and it ranged from 2.7 to 4.1 km/s, but it was always faster than the Chapman–Jouguet (C–J) velocity, to ensure an overdriven detonation condition on the projectile nose. Diaphragms between the ballistic range system and the combustion chamber were either 12- or 50-μm Mylar film. Four different observation locations were used: just behind the Mylar diaphragm, and at 134, 190, and 403 mm downstream. We defined that the initial temperature of the mixture gas was T_0, the initial pressure of the mixture gas was p_0, and the projectile velocity was V_p.

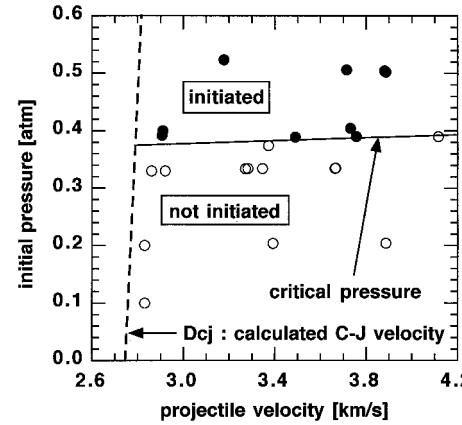

Fig. 2 Critical pressure for sustaining a steady-state C–J detonation wave.

Results and Discussion

Definition of Critical Pressure

We define critical pressure p^* as the minimum initial pressure at which the projectile can initiate and sustain a steady-state C–J detonation wave. Figure 2 shows the dependency of steady-state C–J detonation initiation on the initial pressure of mixture and the projectile velocity. The open circles plot the case where the projectile cannot initiate the detonation (the cases below critical pressure) and the closed circles plot the case where it can initiate (the cases above critical pressure). From Fig. 2, we experimentally determine $p^* = 0.38 \pm 0.02$ atm at $D_{CJ} \leq V_p \leq 4.1$ km/s.

Case Below Critical Pressure

History of Shock Waves Around Hypersonic Projectile

Figure 3 shows schlieren pictures of the projectile flight length from the diaphragm locations of 35 ± 8 mm (Fig. 3a), 134 ± 8 mm (Fig. 3b), 267 ± 30 mm (Fig. 3c), and 442 ± 50 mm (Fig. 3d), where initial fill pressure is below the critical pressure (experimental conditions of Figs. 3 and 4 are shown in Table 1). The white dots are the markers for measuring the projectile location. Each dot is 1 mm wide and is separated 15 mm from the next dot both in the horizontal and vertical directions. The markers are common in all of the schlieren pictures. Because we used negative photographs for clarity, the projectile color is white in those pictures. Figure 4 shows a combination of OH self-emission image (upper half) and schlieren picture (lower half), taken simultaneously.

Before detailed explanation of schlieren and OH emission pictures (Figs. 3 and 4), we summarize the projectile flight history, as shown in Fig. 5. In the first schematic picture (a), when the projectile ruptures the 12-μm Mylar film, the detonation wave structure is composed of three clearly distinguishable waves: 1) an overdriven bow detonation wave surrounding the projectile, which acts as piston, 2) a strong detonation wave formed by the interaction between projectile and diaphragm, and 3) a diffracted shock wave trailing behind the detonation wave. As the projectile proceeds, the second schematic (b) shows how the initially formed strong detonation wave attenuates and becomes a C–J detonation wave (Mach number behind the detonation wave $M_2 > 1$ and normal component of the Mach number $M_{n2} = 1$ moving away from the projectile). Finally, the third schematic (c) shows how the overdriven bow detonation wave surrounding the projectile is attenuated by the rarefaction waves from the projectile shoulder and becomes an overdriven bow detonation wave ($M_2 < 1$, $M_{n2} < 1$) with a reactive bow shock wave trailing (coupled and decoupled shock-induced combustion wave). During this process, the diffracted shock wave propagates downstream at a lower velocity.

We observed these phenomena [Fig. 5 schematics (b) and (c)] as straw-hat type in Ref. 19. However, in Ref. 19, we observed them for only 16 μs by using a multi-framing camera, and the unsteady-state wave propagation was not caught when taking into account experimental errors.

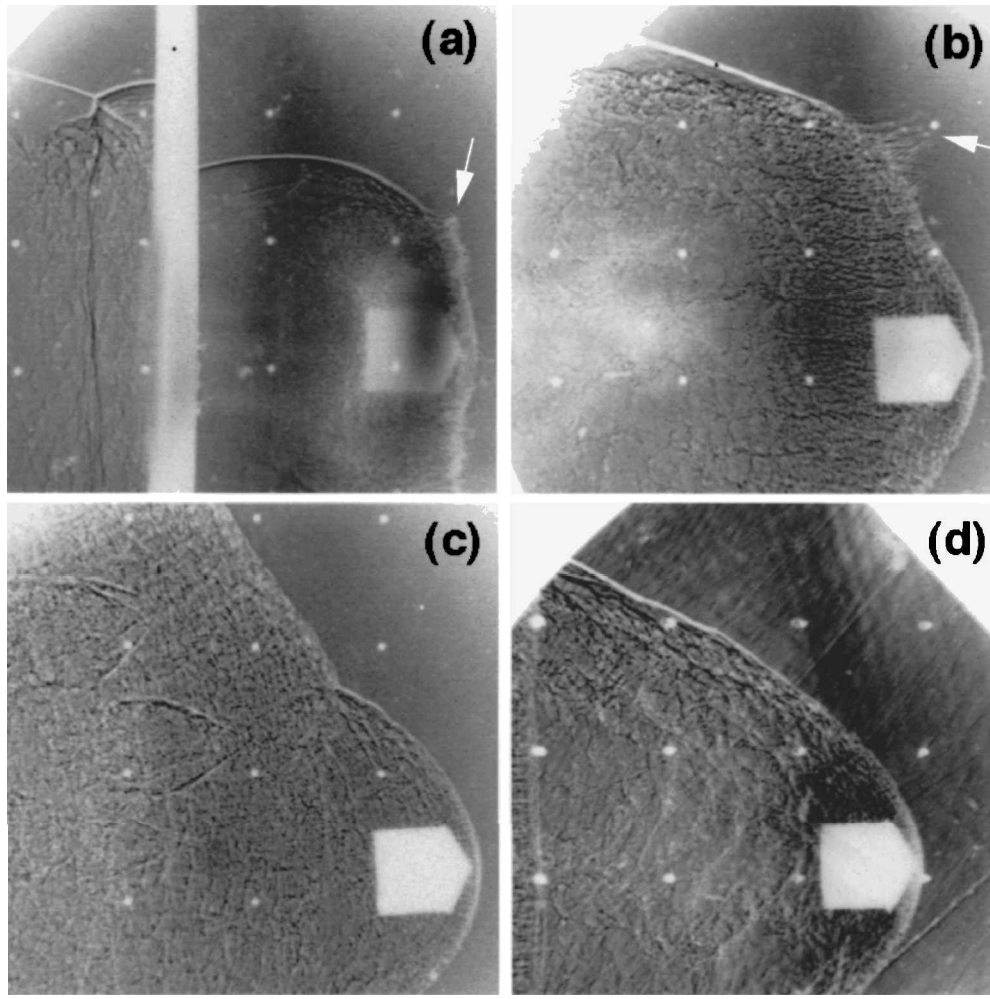

Fig. 3 Case below critical pressure, schlieren picture varying the projectile flight length from diaphragm location: a) 35, b) 134, c) 267, and d) 442 mm.

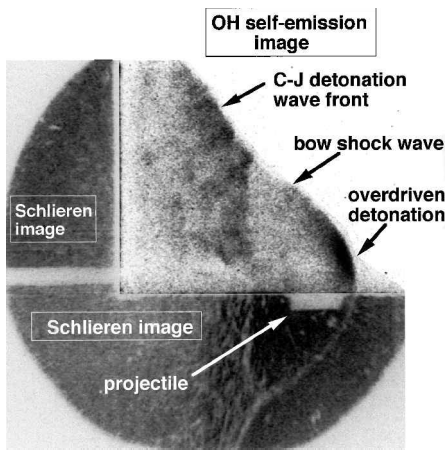

Fig. 4 OH radical self-emission (upper half) plus schlieren picture (lower half) at location 205 (exposure time 200 ns).

Schlieren Pictures at Different Locations

In the following discussion, location X mm means the projectile flight distance, X mm, from the diaphragm location. Figure 3a shows the flowfield around the projectile right after the diaphragm, at location 35 mm. In Fig. 3a, the 7-mm-wide white vertical line is the shadow of the Mylar diaphragm. The thickness is due to the diaphragm not being perfectly flat. A normal shock is observed in front of the projectile. A weak shock wave diffracting from the diaphragm is propagating upward.

In the case at location 134 mm (Fig. 3b), a strong detonation wave is observed in front of the projectile. A weak shock wave diffracting from the diaphragm is extending upward. From Figs. 3a and 3b, it is seen that the strong detonation wave is the result of the interaction between diaphragm, projectile, and bow shock wave. Diaphragm fragments were also observed in Figs. 3a and 3b (white arrows). A lot of diaphragm fragments were launched at very high speed into the combustible gas by the impact of projectile, and cone-shaped weak shock waves (Mach cone) were generated around fragments.

At location 267 mm (Fig. 3c), the strong detonation wave becomes a cone-shaped oblique detonation wave. From the measurement of projectile velocity and detonation angle, the normal velocity of the cone-shaped oblique detonation wave front is close to the theoretical C–J value (where the detonation angle β equals the C–J detonation wave angle β_{CJ}). However, the C–J oblique detonation wave is unsteady relative to the projectile location. Strongly coupled reactive bow shock waves [which were coupled shock-induced combustion wave and strong overdriven detonation wave, as shown Fig. 5 schematic (c)] surround the projectile. This same stage was observed by the OH self-emission method, as shown in Fig. 4. From Fig. 4 we find that a strong OH radical source is established at the projectile tip, where the overdriven detonation wave is generated. Notice how well the position of the C–J oblique detonation front in the OH self-emission picture matches with the position in the schlieren picture, which proves it is a detonation wave. At location 442 mm (Fig. 3d), only the strongly coupled reactive bow shock wave remains; the cone-shaped oblique detonation has disappeared. However, we can still see a vertical line near the left edge of Fig. 3d, which we considered as the border between the C–J oblique detonation wave and the reactive bow shock wave.

We define two characteristic points, A and B. A is the point where the C–J detonation wave and the overdriven bow detonation wave are adjacent, and B is the point where C–J detonation wave and the

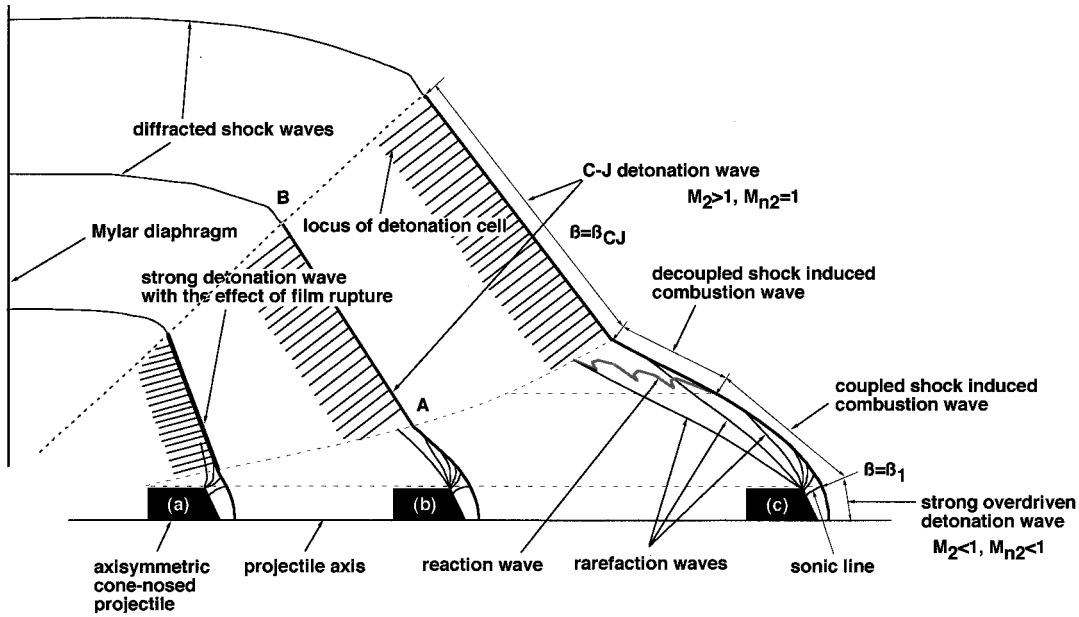

Fig. 5 History of detonation and shock waves around hypersonic projectile (case below critical pressure).

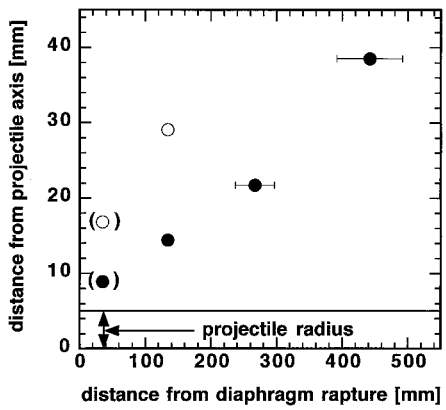

Fig. 6 Loci of the characteristic points: ●, points A, and ○, points B.

diffracted shock wave are adjacent. Figure 6 shows the locations of points A and B. The horizontal axis of Fig. 6 is the projectile flight distance from the diaphragm rupture. The vertical axis of Fig. 6 is the distance from the projectile axis. The loci of the points A and B are almost straight. These data correspond to the cases at $p = 0.33$ atm, except for the two points enclosed in parenthesis, which correspond to $p = 0.20$ atm, but at this pressure the characteristic point location did not depend strongly on the initial pressure.

Case Above Critical Pressure

In the case of supercritical pressure (experimental conditions are shown in Table 1) at location 68 mm (Fig. 7a), the strong detonation wave formed by the diaphragm rupture was observed in front of the projectile, as in the case below the critical pressure. However, the diffracted shock wave became a coupled shock wave (diffracted shock-induced combustion wave). At location 326 mm (Fig. 7b), the strong detonation wave had become a C–J oblique detonation wave connected smoothly to the overdriven bow detonation wave. From other observations around location 326 mm, we found that the detonation phenomena had been steady.

From these experimental results, we concluded that, as shown in Fig. 8, above critical pressures, as the projectile proceeds, the initially formed strong detonation wave attenuates and becomes a C–J detonation wave connected smoothly to the overdriven bow detonation wave immediately after diaphragm rupture.

Steady-State Detonation Wave Structure Around Hypersonic Projectiles

Typical Oblique Detonation Waves Around Projectiles

The typical flowfield around a projectile is shown by a schlieren picture in Fig. 9. The experimental conditions of Fig. 9 were $T_0 = 302.1 \pm 0.4$ K, $p_0 = 0.506 \pm 0.003$ atm, and $V_p = 3.71 \pm 0.24$ km/s. Roughly speaking, shock waves generated around the projectile propagated toward the upper right of the picture, while the shock wave near the projectile remained normal to the projectile nose surface. Within 10 mm from the projectile flight axis, the shock wave was bent, but more than 10 mm from the axis, the shock wave is straight.

OH Radical Self-Emission Measurement

The region near the shock waves was observed by OH self-emission measurement (Fig. 10). This is where the hydrogen–oxygen chemical reaction is occurring. In Fig. 10, the density gradient of the flowfield (left and bottom, schlieren) and the reaction zone (upper right, OH self-emission) were observed simultaneously. The experimental conditions of Fig. 10 were $T_0 = 295.9 \pm 0.4$ K, $p_0 = 0.501 \pm 0.003$ atm, and $V_p = 3.76 \pm 0.19$ km/s. The region where the chemical reaction is occurring matched the place just behind the shock waves, which means that the shock waves observed by the schlieren picture are, without doubt, detonation waves. The strength of the chemical reaction near the projectile is greater than the strength far from it. This shows that the detonation wave near the projectile is overdriven with the projectile acting as a piston.

Normal Velocity Component of the Shock Wave

We measured the normal velocity component of the straight detonation wave. Assuming the phenomena were steady state for the projectile, the normal velocity component of the detonation wave, V_n, was calculated by $V_n = V_p \sin\theta$, where V_p and θ are the projectile velocity and detonation wave angle. From the result of our measurement, as shown in Fig. 11, the normal velocity of the cone-shaped oblique detonation wave agreed with the theoretical C–J value within 10%.

Structure of an Oblique Detonation Wave Initiation by a Hypersonic Projectile

Based on the experimentally observed oblique detonation wave structure, we can attempt to describe the structure in terms of fundamental oblique detonation wave elements. These cases exist for steady, two-dimensional oblique detonation waves, as described by Pratt et al.,[25] and here we assume that each of these fundamental

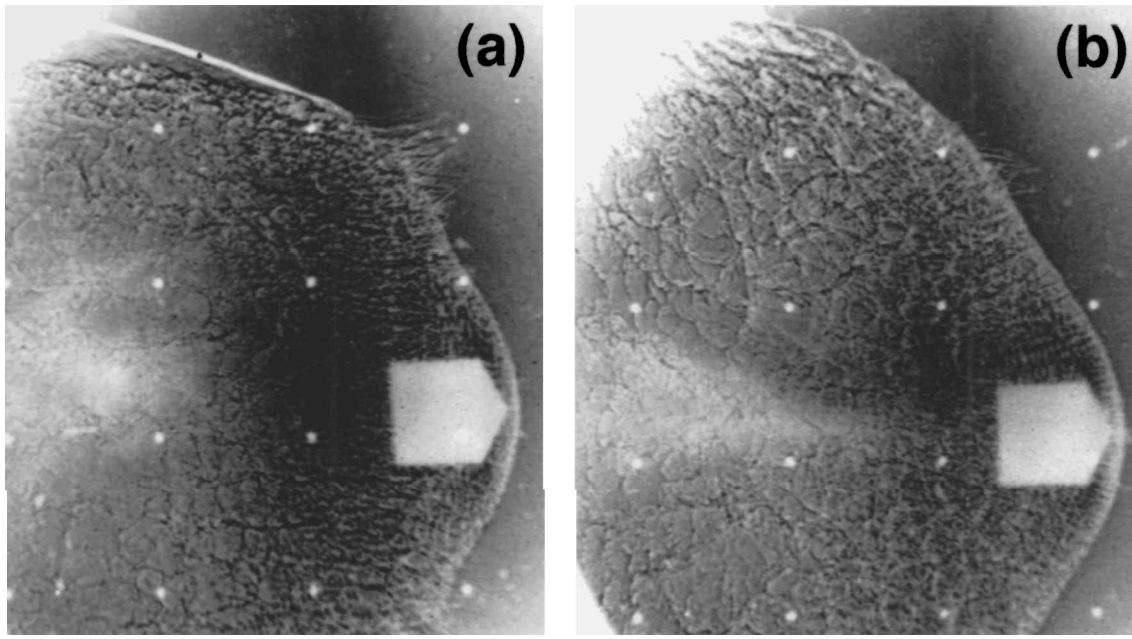

Fig. 7 Case above critical pressure; schlieren pictures varying the projectile flight length from diaphragm location: a) 68 and b) 326 mm.

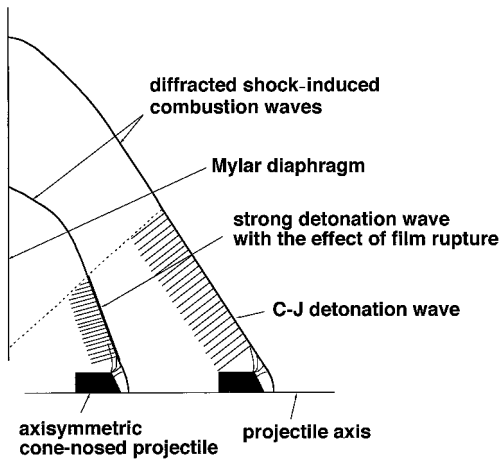

Fig. 8 History of detonation and shock waves around hypersonic projectile (case above critical pressure).

oblique waves applies as a localized structure of the detonation observed around the projectile, as shown in Fig. 12.

1) A strong overdriven detonation wave (SO-DW) is in the subsonic region with a strong compression effect from the projectile face ($M_2 < 1$, $M_{n2} < 1$). At the stagnation streamline, the detonation is normal to the freestream. The flow direction changes little through the detonation wave but suffers a large change along the projectile surface. The flow was compressed and accelerated and finally reaches the sonic speed.

2) A weak overdriven detonation wave (WO-DW) is in the supersonic region with a weak compression effect from the projectile face ($M_2 > 1$, $M_{n2} < 1$). Because the compression effect from the projectile face is weaker than in the case of SO-DW, the shock wave becomes oblique. As a result, although the flow behind the oblique shock wave is supersonic ($M_2 > 1$), the normal velocity component is subsonic ($M_{n2} < 1$). In this region, the rarefaction wave has affected the detonation wave, so that the detonation wave is attenuated and curved. We define β_1 as the detonation angle where the flow behind the detonation wave is sonic, and we divide these regions SO-DW and WO-DW at this point.

3) A quasi-C–J detonation wave (QCJ-DW) is in the sonic region near the projectile, which is strongly affected by the rarefaction wave of the projectile shoulder. With the oblique detonation wave attenuated by the rarefaction wave from the projectile shoulder, the detonation angle decreases, and the flow velocity behind the shock wave increases gradually. The normal velocity component of the flow behind the detonation wave reaches a sonic speed ($M_{n2} = 1$). In this region, the detonation wave has little effect from the rarefaction wave, and so the detonation wave satisfies the C–J conditions. However, in the case of axisymmetric three-dimensional flow, there is actually some effect from the rarefaction wave, and the normal velocity component of the detonation wave is slightly smaller than the C–J velocity (thus labeled a QCJ-DW). In this region the detonation angle also becomes smaller than that of C–J detonation.

4) A C–J detonation wave (CJ-DW) is in the sonic region farthest from the projectile, which is not affected by the rarefaction wave. The characteristic curve of the rarefaction wave is parallel to the detonation wave front far away from the projectile, and there is no effect from the rarefaction wave. The normal velocity component of the detonation wave matches the C–J speed. In this region the detonation angle matches that of a C–J detonation.

Rarefaction Wave of the Projectile Shoulder and Steadiness

The schematic of the detonation wave (Fig. 12) shows the importance of the interaction between the rarefaction waves produced by the projectile shoulder and the detonation front and the effect of the wave curvature.[26] We investigated the fundamental characteristics of the rarefaction wave using the method of characteristics for axisymmetric irrotational flow.[27] We assumed that the initial freestream is parallel to the cone-front surface of the projectile and that its Mach number is homogeneous, M_1. The boundary conditions are a projectile surface and a cone wall boundary, separated by a distance r_p. The specific heat is 1.4. The projectile shoulder has a radius of curvature r.

Figure 13 shows the case of $r = 0.2r_p$. The solution of the characteristics curves does not change when $r < 0.2r_p$. From this calculation, we obtain the characteristic curves of the rarefaction waves from the projectile shoulder. If the inflow Mach number M_1 is changed from 1.1 to 3.0, the directions from the projectile shoulder to the point the rarefaction wave reaches are almost perpendicular to the projectile flight axis (85 ± 11 deg). Figure 14 shows rarefaction waves from the projectile shoulder obtained by the shadowgraph method ($T_0 = 302.6 \pm 0.4$ K, $p_0 = 0.502 \pm 0.003$ atm, and $V_p = 3.89 \pm 0.28$ km/s). The rarefaction wave front (weak discontinuity) is visualized as a curve by the shadowgraph method (the right curve indicated as a rarefaction wave in Fig. 14). The center and right curves indicated as rarefaction waves in Fig. 14 were characteristic lines generated by small disturbances at the projectile surface. Although the accuracy of the projectile position is ± 0.3 mm, the shape

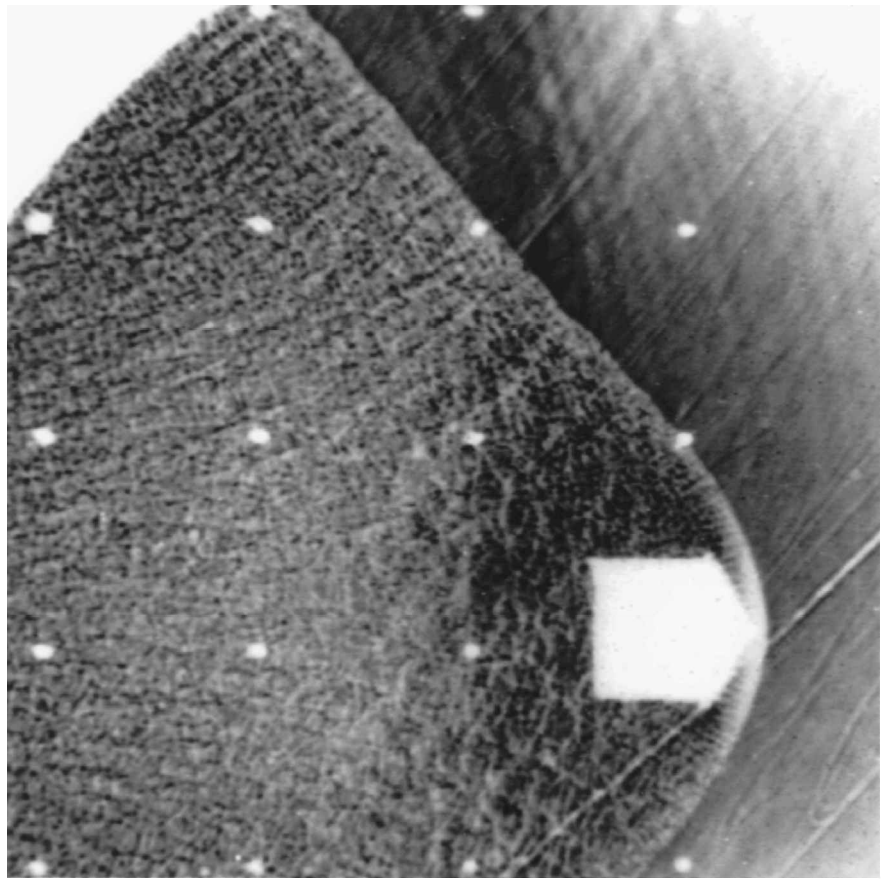

Fig. 9 Typical steady-state oblique detonation wave around hypersonic projectile.

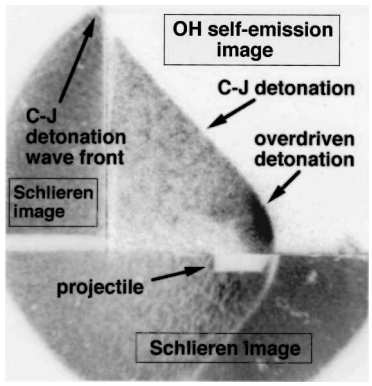

Fig. 10 OH self-emission and schlieren pictures taken simultaneously.

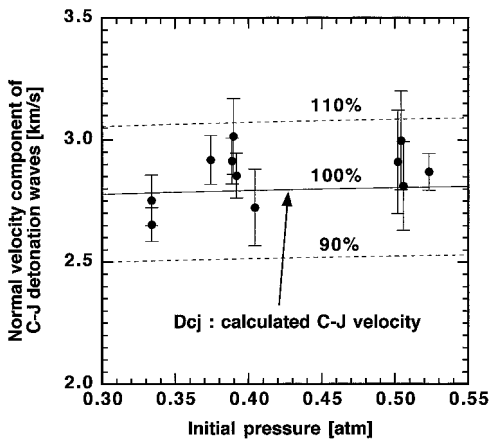

Fig. 11 Normal velocity components of the oblique detonation waves satisfy the C–J condition.

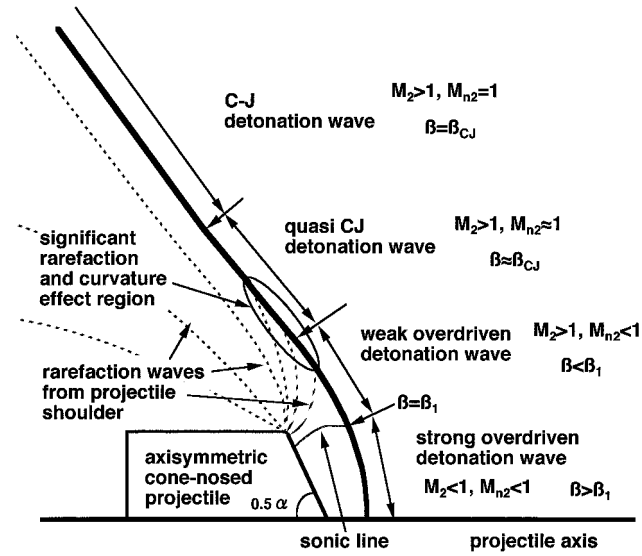

Fig. 12 Oblique detonation structure around hypersonic projectiles.

of the rarefaction waves in Fig. 14 is identical to those of Fig. 13. We confirmed that the effect of the rarefaction wave is more important closer to the projectile shoulder.

Boundary Wall Effect

Figure 15 shows the detonation wave reinitiation right behind a film (Mylar) a priori having a 20-mm-diam circular hole centered in the projectile flight axis. Because the film had the hole, both upstream and downstream of the film were filled with a $2H_2 + O_2$ mixture, with $P_0 = 0.505 \pm 0.003$ atm and $T_0 = 298.3 \pm 0.4$ K. The projectile velocity was 3.67 ± 0.12 km/s. Before the projectile passing the film, the projectile has already generated steady-state C–J

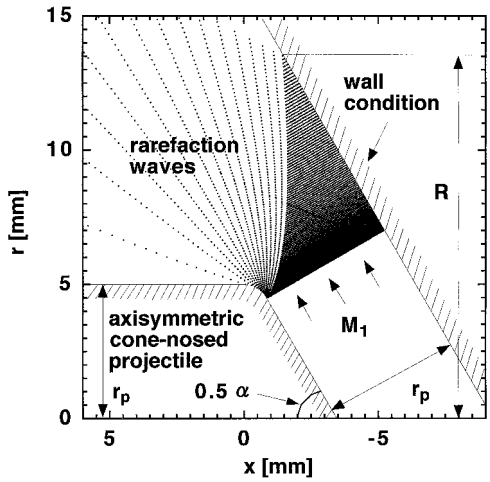

Fig. 13 Numerical calculation of rarefaction waves from the projectile shoulder using the method of characteristics for axisymmetric flow.

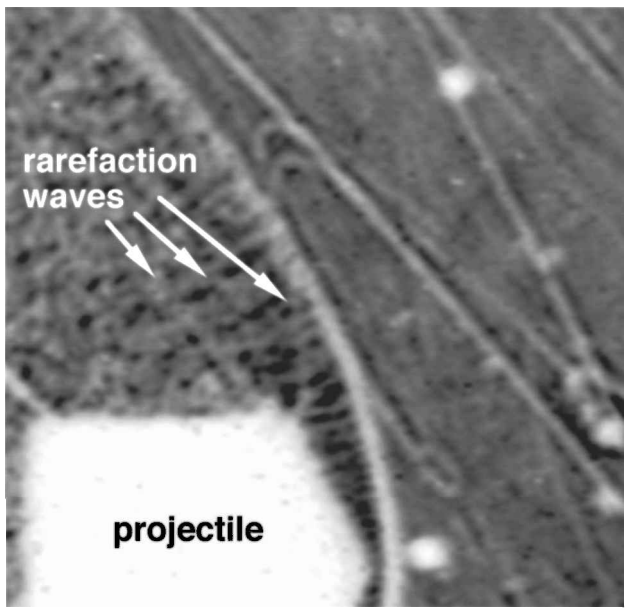

Fig. 14 Rarefaction waves from projectile shoulder (shadowgraph picture).

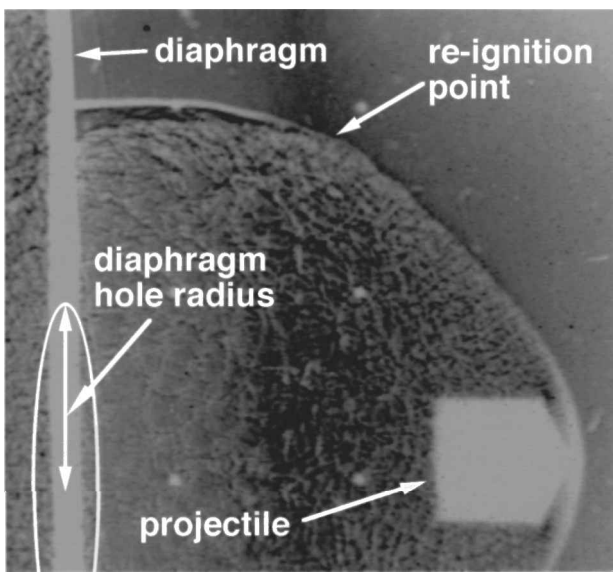

Fig. 15 Diffraction and reinitiation of the oblique detonation waves.

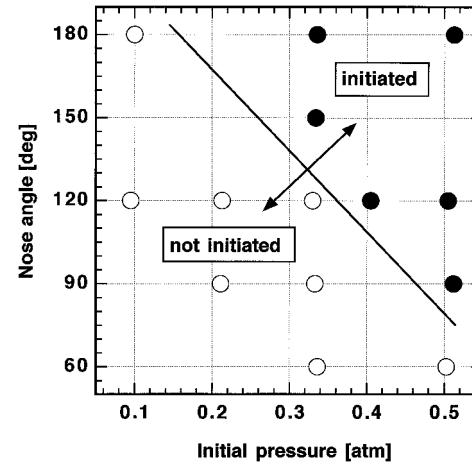

Fig. 16 Dependency of initial pressure and projectile-nose angle (varied).

and quasi-C–J detonation waves (CJ-DW and QCJ-DW) such as shown in Fig. 9. When the projectile passed the film, QCJ-DW was diffracted and once decayed. However, as shown Fig. 15, after the projectile passing the film, the steady-state QCJ-DW was reinitiated around the projectile without help of the boundary wall of the combustion chamber. Thus, we conclude that the boundary wall is not necessary for sustaining steady-state QCJ-DW.

Dependency on Initial Pressure and Projectile-Nose Angle

Figure 16 shows the dependency of steady-state detonation initiation on the initial pressure of the mixture and the projectile-nose angle. The open circles plot the case where projectile cannot initiate the detonation and closed circles for the case where it can initiate. Projectile velocities were almost constant (2.86 ± 0.13 km/s). From these results, we found that steady-state detonation waves will be initiated when initial pressure is high and projectile-nose angle is large enough. Because the nose angle of a projectile is larger, the rate of work done on the mixture gas by the projectile become larger, and then the gas is given large energy density. Because the initial pressure of the mixture is higher, the induction length behind the shock wave is shorter, and the interaction between the shock wave and combustion wave is stronger. From these effects, the high rate of work and the short induction length, the steady-state detonation waves can be generated in the right-upper region of Fig. 16. In the case with high nose angle and high initial pressure of mixture, a SO-DW is generated in front of the projectile tip. Then the SO-DW propagates in the radial direction, is not attenuated by rarefaction waves, and becomes CJ-DW at a location far from the projectile. That is, in such a case, the steady-state oblique detonation waves can appear around projectiles.

Dependency of Projectile Velocity

Schlieren pictures of Fig. 17 show the changes of phenomena when only the projectile velocity varies at near a critical pressure condition. The experimental condition is shown in Table 2. The exposure time of the gate ICCD camera is 50 ns. Figure 17b is the case of typical steady-state oblique detonation (same as Fig. 9). Figure 17a is the lower velocity case, Figs. 17c and 17d are higher velocity cases than the typical case (Fig 17b). In Fig. 17, the projectile lengths are different due to the velocity control in two-stage light-gas gun launching

In the lower velocity case (Fig. 17a), SO-DWs directly connect to CJ-DW without QCJ-DW. In one higher velocity case (Fig. 17c), the QCJ-DW region is wider, and the CJ-DW is located farther from the projectile. From these experimental results, as the projectile velocity increases, the location of the CJ-DW moves farther away. In the other higher velocity case (Fig. 17d), there are no CJ-DWs within the observation region. In this case, the detonation wave is curved throughout the observed region. The detonation angle farthest from the projectile is 20 deg and the interaction between the shock wave and heat release region is weak (decoupled shock-induced combustion).

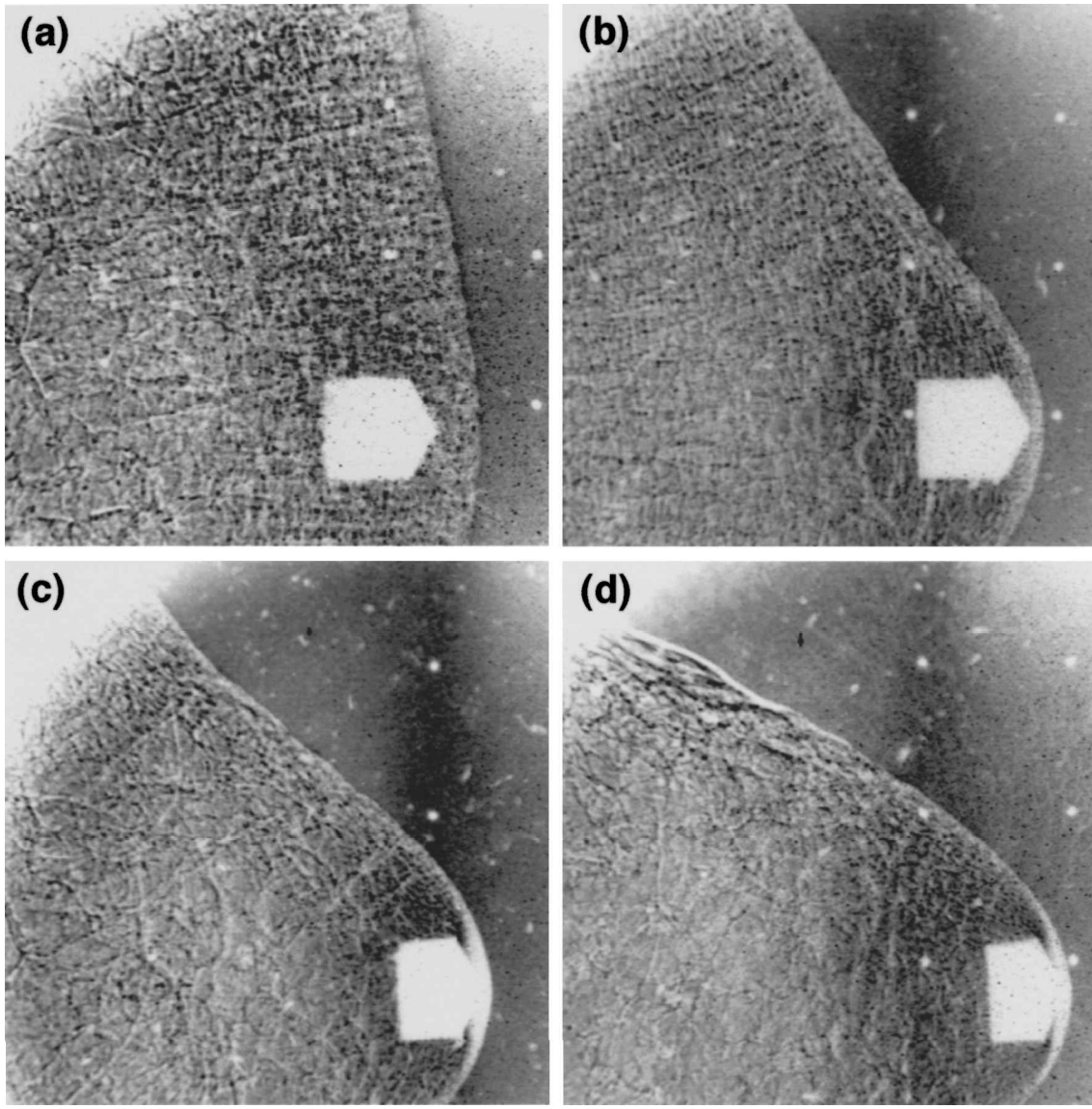

Fig. 17 Projectile velocity dependence; projectile velocity varied from 2.9 to 4.1 km/s (exposure time 50 ns).

As a result, it indicates that the steady-state CJ-DW does not appear in the high-velocity region.

Conclusions

At the pressure condition below the criteria for the steady detonation initiation around a hypersonic projectile, the detonation structure is composed of three different shock and detonation waves, which appear just after a diaphragm rupture and evolve in time: an overdriven bow detonation wave, a strong detonation wave, and a diffracted shock wave. We investigated their propagation after diaphragm rupture and found that the C–J detonation wave moves away from the projectile and only a reactive bow shock wave remained around the projectile far away from the diaphragm. At the pressure condition above the criteria for initiation, the steady oblique detonation wave was generated around the projectile immediately after diaphragm rupture.

We propose the theoretical mechanism of the steady oblique detonation wave that explains the generation and physical characteristics of the detonation wave. We subdivide the detonation wave structure into four parts based on the interaction level and Mach number just behind the wave front. The four parts are 1) a strong overdriven wave in the subsonic region, with a strong compression effect from the projectile face; 2) a weak overdriven wave in the supersonic region, with a weak compression effect from the projectile; 3) a QCJ-DW in the sonic region near the projectile, which is strongly affected by the expansion wave from the projectile shoulder; and 4) a CJ-DW in the sonic region farthest from the projectile, which is not affected by the expansion wave. This mechanism shows the importance of the interaction between the rarefaction waves produced by the projectile shoulder and the detonation front, and its effect on the wave curvature.

Acknowledgments

This work was made possible by a grant from a Japan Society for the Promotion of Science Research Fellowship for Young Scientists. The authors gratefully acknowledge K. Nishide, D. Yahata, J. E. Leblanc, and N. Yoshikawa of Nagoya University for providing help in the experimental works and numerous suggestions.

References

[1] Zeldovich, Y. B., and Leipunsky, O., "A Study of Chemical Reactions in Shock Waves," *Acta Physicochimica U.R.S.S. (Journal of Experimental and Theoretical Physics),* Vol. 18, 1943, pp. 167–171.

[2] Ruegg, F. W., and Dorsey, W. W., "A Missile Technique for the Study of Detonation Waves," *Journal of Research of the National Bureau of Standards, Section C: Engineering and Instrumentation,* Vol. 66C, No. 1, 1962, pp. 51–58.

[3] McVey, J. B., and Toong, T. Y., "Mechanism of Instabilities of Exothermic Hypersonic Blunt-Body Flows," *Combustion Science and Technology*, Vol. 3, 1971, pp. 63–76.

[4] Lehr, H. F., "Experiments on Shock-Induced Combustion," *Astronautica Acta*, Vol. 17, 1972, pp. 589–597.

[5]Alpert, R. L., and Toong, T. Y., "Periodicity in Exothermic Hypersonic Flows about Blunt Projectiles," *Astronautica Acta*, Vol. 17, 1972, pp. 539–560.

[6]Matsuo, A., and Fujii, K., "Prediction Method of Unsteady Combustion Around Hypersonic Projectile in Stoichiometric Hydrogen–Air," *AIAA Journal*, Vol. 36, No. 10, 1998, pp. 1834–1841.

[7]Matsuo, A., and Fujii, K., "Detailed Mechanism of the Unsteady Combustion Around Hypersonic Projectiles," *AIAA Journal*, Vol. 34, No. 10, 1996, pp. 2082–2089.

[8]Kamel, M. R., Morris, C. I., Hanson, R. K., "Simulation PLIF and Schlieren Imaging of Hypersonic Reactive Flows Around Blunted Cylinders," AIAA Paper 97-0913, 1997.

[9]Viguier, C., Guerraud, C., and Desbordes, D., "H_2–Air and CH_4–Air Detonations and Combustions behind Oblique Shock Waves," *Proceedings of the Twenty-Fifth Symposium (International) on Combustion*, Combustion Inst., Pittsburgh, PA, 1994, pp. 53–59.

[10]Desbordes, D., Hamada, L., and Guerraud, C., "Supersonic H_2–Air Combustion behind Oblique Shock Waves," *Shock Waves*, Vol. 4, 1995, pp. 339–345.

[11]Li, C., Kailasanath, K., and Oran, E. S., "Detonation Structure behind Oblique Shocks," *Physics of Fluids*, Vol. 6, No. 4, 1994, pp. 1600–1611.

[12]Higgins, A. J., "The Effect of Confinement on Detonation Initiation by Blunt Projectiles," AIAA Paper 97-3179, July 1997.

[13]Higgins, A. J., and Bruckner, A. P., "Experimental Investigation of Detonation Initiation by Hypervelocity Blunt Projectiles," AIAA Paper 96-0342, Jan. 1996.

[14]Higgins, A. J., "Investigation of Detonation Initiation by Supersonic Blunt Bodies," Ph.D. Dissertation, Dept. of Aeronautics and Astronautics, Univ. of Washington, Seattle, WA, 1996.

[15]Lee, J. H. S., "Initiation of Detonation by a Hypervelocity Projectile," *Advances in Combustion Science: In Honor of Ya. B. Zel'dovich*, edited by W. A. Sirignano, A. Merzhanov, and L. De Luca, Vol. 173, Progress in Astronautics and Aeronautics, AIAA, Reston, VA, 1997, pp. 293–310.

[16]Kaneshige, M. J., and Shepherd, J. E., "Oblique Detonation Stabilized on a Hypervelocity Projectile," *Proceedings of the Twenty-Sixth Symposium (International) on Combustion*, Combustion Inst., Pittsburgh, PA, 1996, pp. 3015–3022.

[17]Kasahara, J., Horii, T., Endo, T., and Fujiwara, T., "Experimental Observation of Unsteady H_2–O_2 Combustion Phenomena Around Hypersonic Projectiles Using a Multiframe Camera," *Proceedings of the Twenty-Sixth Symposium (International) on Combustion,* Combustion Inst., Pittsburgh, PA, 1996, pp. 2903–2908.

[18]Kasahara, J., Horii, T., Endo, T., and Fujiwara, T., "Unsteady Combustion and Oblique Detonation Induced by Hypersonic Projectiles Flying in Hydrogen–Air Mixtures," *Journal of the Japan Society for Aeronautical and Space Science*, Vol. 45, No. 517, 1997, pp. 102–109.

[19]Kasahara, J., Takeishi, A., Kuroda, H., Horiba, M., Matsukawa, K., Leblanc, J. E., Endo, T., and Fujiwara, T., "Experimental Observation of Oblique Detonation Waves around Hypersonic Free Projectiles," *Ram Accelerators*, edited by K. Takayama and A. Sasoh, Springer-Verlag, Heidelberg, Germany, 1998, pp. 263–270.

[20]Kailasanath, K., "Applications of Detonations to Propulsion: A Review," AIAA Paper 99-1067, June 1999.

[21]Hertzberg, A., Bruckner, A. P., and Bogdanoff, D. W.,"Ram Accelerator: A New Chemical Method for Accelerating Projectiles to Ultrahigh Velocities," *AIAA Journal*, Vol. 26, No. 2, 1988, pp. 195–203.

[22]Powers, J. M., "Oblique Detonations: Theory and Propulsion Applications," *Combustion in High-Speed Flows*, edited by J. Buckmaster, T. L. Jackson, and A. Kumar, Kluwer Academic, The Netherlands, 1994, pp. 345–371.

[23]Bussing, T., and Pappas, G., "Pulse Detonation Engine Theory and Concepts," *Developments in High-Speed-Vehicle Propulsion Systems*, edited by S. N. B. Murthy and E. T. Curran, Vol. 165, Progress in Astronautics and Aeronautics, AIAA, Reston, VA, 1996, pp. 421–472.

[24]Chang, X., Hemmi, M., Sasoh, A., and Fujiwara, T., "An Experimental Study on Hypersonic Flow Using a Ballistic Range (I) Photographic Measurement and Its Processing," *Journal of the Japan Society for Aeronautical and Space Science*, Vol. 41, No. 81, 1993, pp. 519–528.

[25]Pratt, D. T., Humphrey, J. W., and Glenn, D. E., "Morphology of Standing Oblique Detonation Waves," *Journal of Propulsion and Power*, Vol. 7, No. 5, 1991, pp. 837–845.

[26]Yao, J., and Stewart, D. S., "On the Normal Detonation Shock Velocity-Curvature Relationship for Materials with Large Activation Energy," *Combustion and Flame*, Vol. 100, 1995, pp. 519–528.

[27]Anderson, J. D., Jr., *Modern Compressible Flow with Historical Perspective*, McGraw–Hill, New York, 1982, pp. 282–286.

K. Kailasanath
Associate Editor